Hybrid humic acid/titanium dioxide nanomaterials as highly effective antimicrobial agents against gram(-) pathogens and antibiotic contaminants in wastewater

Giuseppe Vitiello[a,b,*], Virginia Venezia [a], Mariavittoria Verrillo[c], Assunta Nuzzo[c], Judith Houston [d], Stefano Cimino[e], Gerardino D'Errico[b, f], Antonio Aronne[a], Luigi Paduano[b,f], Alessandro Piccolo[c], Giuseppina Luciani[a]

[a] Department of Chemical, Materials and Production Engineering (DICMaPI), University of Naples Federico II, Piazzale Tecchio 80, 80125 Naples, Italy.

[b] CSGI, Center for Colloid and Surface Science, via della Lastruccia 3, Sesto Fiorentino (FI), Italy.

[c] Department of Agricultural Science, University of Naples Federico II, via Università 100, 80055 Portici, Italy and Centro Interdipartimentale di Ricerca sulla Risonanza Magnetica Nucleare per l'Ambiente, l'Agro-Alimentare ed i Nuovi Materiali (CERMANU) via Università 100, 80055 Portici, Italy.

[d]Jülich Centre for Neutron Science (JCNS) at Heinz Maier-Leibnitz Zentrum (MLZ), Forschungszentrum Jülich GmbH, Lichtenbergstraße 1, Garching, 85747, Germany and European Spallation Source (ESS), Odarslövsvägen 113, 225 92 Lund, Sweden.

[e] IRC-Istituto di Ricerche sulla Combustione, CNR - Consiglio Nazionale delle Ricerche, Piazzale V. Tecchio 80, 80125 Naples, Italy.

[f] Department of Chemical Sciences, University of Naples Federico II, via Cinthia 4, 80126 Naples, Italy.

*_corresponding author_: giuseppe.vitiello@unina.it,Tel: +39 081 7685975 fax: +39 081 7682595

Abstract

Humic acids (HAs) provide an important bio-source for redox-active materials. Their functional chemical groups are responsible for several properties, such as metal ion chelating activity, adsorption ability towards small molecules and antibacterial activity, through reactive oxygen species (ROS) generation. However, the poor selectivity and instability of HAs in solution hinder their application. A promising strategy for overcoming these disadvantages is conjugation with an inorganic phase, which leads to more stable hybrid nanomaterials with tuneable functionalities. In this study, we demonstrate that hybrid humic acid/titanium dioxide nanostructured materials that are prepared via a versatile *in situ* hydrothermal strategy display promising antibacterial activity against various pathogens and behave as selective sequestering agents of amoxicillin and tetracycline antibiotics from wastewater. A physicochemical investigation in which a combination of techniques were utilized, which included TEM, BET, ^{13}C-CPMAS-NMR, EPR, DLS and SANS, shed light on the structure-property-function relationships of the nanohybrids. The proposed approach traces a technological path for the exploitation of organic biowaste in the design at the molecular scale of multifunctional nanomaterials, which is useful for addressing environmental and health problems that are related to water contamination by antibiotics and pathogens.

Keywords: nanohybrids; biowaste valorisation; humic substances; titanium dioxide; reactive oxygen species (ROS); antibacterial; wastewater remediation.

1. Introduction

The waste-to-wealth concept aims at encouraging a future sustainable lifestyle in which waste and biowaste valorisation is considered not only for its intrinsic environmental benefits but also to prompt the development of new technologies and jobs. To help rethink planetary well-being in terms of a circular economy, the main objective is to promote strategies for enhancing the economic and environmental value of biowaste through its recycling or conversion (Xu et al. 2019). Biowaste can be drastically transformed, either chemically, physically or biologically, into a plethora of end-use products and functional novel materials via several approaches.

In this context, humic acids (HAs) are an alkali-soluble fraction of natural organic matter, which are usually found in water, soil and sediments. They play central roles in sustaining plant growth and controlling both the fate of environmental pollutants and the biogeochemistry of organic carbon in global ecosystems (Maccarthy, 2001; Piccolo et al., 2019; Stevenson et al., 1994). They can be obtained via biomass conversion through natural biological transformations and are unavoidable co-products in biorefinery processes (Luo et al., 2019; Spaccini et al.,2019). Additionally, HAs are considered a promising and inexpensive source of novel materials for technological applications (de Melo et al., 2016; Dutta et al., 2019; Peña-Méndez et al., 2005; Perminova et al., 2019). HAs are attracting substantial interest as heterogeneous organic molecules due to their carbogenic diversity and tuneable redox properties, thereby providing an important source of inspiration for novel redox-active materials (de Melo et al., 2016; Nuzzo et al., 2013). Indeed, HAs present various functional groups in their chemical structures, such as quinone, phenol, carboxyl and hydroxyl moieties, which are directly responsible for regenerable redox properties (de Melo et al., 2016; Klüpfel et al., 2014). These properties enable HAs to generate or scavenge reactive oxygen species (ROSs) (Aeschbacher et al. 2012; de Melo et al., 2016; Scott et al. 1998), thereby leading to various properties, such as antibacterial, antioxidant and anti-inflammatory activities (van Rensburg et al. 2000; de Melo et al., 2016). Furthermore, they can easily act as metal chelating agents (Li et al., 2020) due to their amphiphilicity, which determines their self-assembly (Klavins et al., 2020; Nuzzo et al., 2013;

Piccolo, 2001), and they can interact with contaminants (Afzal et al., 2019; Du et al., 2020; Liu et al., 2020). Considering these properties, HAs are expected to play a leading role in green chemistry as an accessible and inexpensive source for the design and development of multifunctional materials for potential bio-sustainable applications. HAs from North Dakota leonhardite (NDL) have attracted interest due to their low cost and marked amphiphilicity (Cozzolino et al., 2002; Nuzzo et al., 2016). The latter is due to the large amounts of both hydrophobic and hydrophilic functionalities within the humic components, such as fatty and phenolic residues (Drosos et al., 2017; Nebbioso et al., 2011). Despite the substantial potential that is offered by bioavailable HA-like materials, several challenges remain to be overcome, which are related mainly to their poor selectivity and high instability (browning) under aerated conditions (Allard et al., 1994). Although intense research has focused on the production of radicals and trapping reactions of low-molecular-weight natural phenol-like derivatives, much less attention has been given to their possible exploitation in materials science. Moreover, although many studies on interactions between HAs and pollutants have been proposed, the difficulty in distinguishing between soluble and insoluble HAs often hinders the assessment of their adsorption features (Afzal et al., 2019; Du et al., 2020). HAs have shown high solubility in aqueous media, thereby preventing the possibility of efficiently removing pollutants from aqueous environments. HAs are controversial moieties since their interactions with nanomaterials and organic pollutants can increase the solubility and bio-persistence of these species in aqueous solutions (de Melo et al., 2016). Consequently, the non-negligible chemical lability and heterogeneous self-assembly behaviour of HAs strongly prevent the full exploitation of these intriguing biomacromolecules, which are often regarded as an environmental issue rather than a valuable resource due to their abundance and their function as carriers of pollutants. In this context, a promising strategy for overcoming these disadvantages was proposed based on the conjugation of HA-organic moieties onto a foreign matrix that consisted of either organic or inorganic materials (de Oliveira et al., 2016). Inorganic nanoparticles have been highlighted as attractive bio-interfaces due to their biocompatibility and their tuneable size, shape and porosity with functional versatility and, therefore,

are valid candidates for the realization of multifunctional nanomaterials with modulable properties (de Oliveira et al., 2016; Heuer-Jungemann et al., 2019; Luchini et al., 2019). Recently, following a bioinspired approach, we proposed a novel synthetic strategy for producing hybrid nanostructures, whereby a titanium dioxide (TiO_2) sol acts as a catalyst and templating agent for 5,6-dihydroxyindole-2-carboxylic acid (DHICA) polymerization to eumelanin (Pezzella et al., 2013; Vitiello et al., 2015; Vitiello et al., 2016). The inorganic phase has a tuned eumelanin supramolecular structure, which leads to TiO_2-eumelanin hybrids with unique antimicrobial properties that are sensibly better than the intrinsic melanin biocide activity (Vitiello et al., 2015; Vitiello et al., 2017; Vitiello et al., 2018). The combination of biomacromolecules and inorganic components into a hybrid nanostructure at the molecular scale has proven to be an extremely effective strategy for enhancing the intrinsic properties of the organic phase and selectively driving its function (Silvestri et al. 2019; Vitiello et al. 2019). On this basis, TiO_2 can be proposed as a biomimetic templating agent for controlling and modulating the stability and reactivity of HAs, including the ROS production ability, the sequestering capability towards metal cations and organic pollutants and the size-selective absorption features (de Melo et al., 2016; Tang et al., 2014). Additionally, due to the amphiphilicity of their supramolecular structure (Piccolo, 2001), HAs can favourably interact with an inorganic surface charged phase through electrostatic forces and can confer satisfactory colloidal stability in aqueous media (Pota et al., 2020; Zhang et al., 2020).

In this paper, hybrid humic acid/titanium dioxide nanostructures were designed and prepared through an *in situ* method that was based on the hydrothermal wet chemistry approach. Then, the functionality of these novel nanohybrids was investigated, and two main applications for water remediation were considered: i. antibacterial activity against gram-negative and gram-positive pathogens of various strains and ii. sequestering action towards three antibiotics, namely, amoxicillin, tetracycline and metronidazole, in an aqueous solution. To shed light on the relationship between the structural and functional features of the nanohybrids, a wide physicochemical investigation was conducted via a combined approach of various techniques, such as transmission electron microscopy (TEM), X-ray

diffraction (XRD), thermogravimetry (TG), BET porosimetry, dynamic light scattering (DLS), small-angle neutron scattering (SANS), Fourier-transform infrared (FT-IR) spectroscopy, solid-state cross-polarization magic angle spinning carbon-13 nuclear magnetic resonance (13C-CPMAS-NMR) spectroscopy and electron paramagnetic resonance (EPR) spectroscopy. These analyses enable the investigation of the effects at the molecular scale of the combination of HA and TiO_2 components in defining the structural, surface and paramagnetic properties of the final TiO_2/HA-NDL nanohybrids and in modulating both ROS generation for killing bacteria and the removal of antibiotics from wastewater.

Overall, this study defines a potential strategy for converting environmental challenges that are posed by the interaction of HAs with organic pollutants and inorganic nanoparticles into a technological opportunity through the design of hybrid multifunctional nanomaterials. This approach offers the opportunity to match the objectives of giving biowaste a new life and managing water quality through pharmaceutical removal and pathogen disinfection, thereby addressing current environmental and health concerns.

2. Materials and Methods

2.1 Materials

Titanium(IV) isopropoxide (TTiP, purity ≥ 99.9%), 2-propanol (purity ≥ 99.5%), acetic acid (purity ≥ 99.85%), triethylamine (TEA, purity ≥ 99.5%), 5,5-dimethyl-1-pyrroline-1-oxide (DMPO) spin-trap and D_2O solvent (99.9% purity) were purchased from Sigma-Aldrich (Milan, Italy). Humic acids that were obtained from North Dakota leonardite were made available by Mammoth International Chemical Corporation (Houston, TX, USA). Amoxicillin (potency: ≥ 900 $\mu g \cdot mg^{-1}$), tetracycline (potency: ≥ 850 $\mu g \cdot mg^{-1}$) and metronidazole (potency: ≥ 0.21 μM) antibiotics were obtained from Mylan (Milan, Italy), Scharper (Milan, Italy) and Teofarma (Valle Salimbene, Pv, Italy), respectively. All reagents were used without further purification.

2.2 Synthesis of hybrid TiO_2/HA-NDL nanostructures.

TiO_2 and hybrid TiO_2 nanostructures were prepared in the absence and presence, respectively, of humic acid (HA). The HAs were extracted from North Dakota leonardite (HA-NDL) and purified via common procedures, as described elsewhere (Piccolo et al., 2005). The average molecular weight (*Mwa*) of the purified HA was 1470 ± 60 Da (Piccolo et al., 2005), and its elemental content and solid-state NMR spectrum were reported earlier (Piccolo et al., 2019). The synthesis was conducted via a hydrothermal process that was based on an experimental procedure that was previously developed by our group for producing antimicrobial hybrid melanin-based nanomaterials (Vitiello et al., 2015; Vitiello et al., 2017). Various molar ratios of the organic and inorganic components were used to evaluate the effects of the amount of the organic component on the structural and functional properties of the final hybrid nanostructures. First, a solution of the TiO_2 precursor was prepared via dropwise addition of 6 mL of 1.69 M titanium(IV) isopropoxide (TTiP) in 2-propanol to 31.3 mL of an aqueous solution of acetic acid at pH=1.5. This mixture was stirred for two days, and a TiO_2 colloidal suspension was obtained. Then, suitable amounts of HA-NDL were added to the TiO_2-sol suspension to produce four ratios: 0.1, 0.2, 1.0 and 2.0 mmol HA-NDL/mol TTiP (Table 1). Subsequently, triethylamine (TEA) was added dropwise to the mixtures until pH=7.0. Then, the obtained suspensions were sealed within Teflon recipients, in which the liquid volume corresponded to 75% of the total volume, and they were placed into a circulating oven and maintained at 120 °C for 18 hours. The final samples were obtained by centrifugation at 12500 rpm for 15 min and washing 3 times with distilled water.

Table 1. Molar ratios of the organic and inorganic precursors that were used for the synthesis of TiO_2/HA-NDL nanohybrids.

nanohybrid sample	***nominal composition HA:Ti (mmol:mol)***
TiO_2/HA-NDL_0.1	1:10
TiO_2/HA-NDL_0.2	1:5
TiO_2/HA-NDL_1	1:1
TiO_2/HA-NDL_2	2:1

The obtained precipitates were resuspended in doubly distilled water to obtain four stable suspensions, which were named TiO_2/HA-NDL_0.1, TiO_2/HA-NDL_0.2, TiO_2/HA-NDL_1 and TiO_2/HA-NDL_2.

2.3 Physicochemical investigation

A multi-perspective, physico-chemical investigation of the TiO_2/HA-NDL nanostructures was conducted via a combined approach of complementary techniques to obtain detailed information on their chemical, morphological and surface properties and on their structural organization.

X-ray diffraction (XRD) experiments were conducted with a Malvern PANalytical diffractometer (Malvern, United Kingdom) with a nickel filter and Cu Kα radiation to investigate the crystalline phases of the TiO_2 component within the final hybrid nanostructures.

The weight loss of the dried samples, along with the presence of HA-NDL in the hybrid samples, was evaluated using a TA Instrument simultaneous thermo-analyser (SDT Q600, New Castle, Delaware, USA) by following a previously described procedure (Melone et al., 2019; Pezzella et al., 2013). TG/DTA tests were conducted on 20 mg dried specimens in air (temperature range: from room temperature to 800 °C; heating rate: 10 °C min^{-1}).

An FT-IR investigation was conducted by using a Nicolet Instrument Nexus model (Thermo Scientific, Waltham, MA, USA) that was equipped with a DTGS KBr (deuterated triglycine sulfate with potassium bromide windows) detector. IR absorption spectra were recorded in the 4000-400 cm^{-1} range at a resolution of 2 cm^{-1} on pressed disks of powders that had been previously diluted in KBr (1 wt%). The IR spectrum of each sample was corrected based on a spectrum of blank KBr.

The solid-state ^{13}C-CPMAS-NMR spectra of pure HA-NDL and TiO_2/HA-NDL nanohybrids were acquired with a 300 MHz Bruker Avance wide-bore magnet (Bruker Bio Spin GmbH, Rheinstetten, Germany) that was equipped with a CPMAS probe: Into 4 mm zirconia rotors, 90 mg of each sample was loaded. The rotors were closed with Kel-F caps and spun at a rate of 10000 ± 1 Hz, and 32000 scans were acquired. Then, HA-NDL samples before and after hydrothermal treatment were dissolved

in deuterated H_2O and analysed with a 400 MHz Bruker Avance magnet (Bruker BioSpin GmbH, Rheinstetten, Germany) that was equipped with a ^{1}H-BBI probe; 128 scans were conducted. The spectra were processed by using both the Bruker Topspin software (v2.1, BrukerBiospin, Rheinstetten, Germany) and the MNOVA software (v.9.0, Mestrelab Research, Santiago de Compostela, Spain) (Mazzei et al., 2016).

Morphological properties were investigated via TEM: Samples were prepared by placing a drop of the nanohybrid suspension on one side of a 200 mesh copper grid. TEM images were obtained using an FEI TECNAI G^2 200 kV microscope (Thermo Fisher Scientific, Waltham, USA) that was equipped with a high-angle annular dark-field (HAADF) detector for high-resolution imaging.

The surface properties were determined via N_2 adsorption at -196 °C starting from $P/P_0=5\times10^{-6}$ using a Quantachrome Autosorb 1-C instrument (Quantachrome, Anton Paar Italia, Rivoli, Italy). Before the analysis, the samples were degassed under high vacuum at 120 °C for 4 h. The BET method (P/P_0 range from 0.08 to 0.3) was adopted for the calculation of the specific surface area (S_{BET}), while the total pore volume (V_{TOT}) was computed using Gurvitsch's rule (at $P/P_0=0.995$). Finally, the pore size distribution was evaluated via application of the BJH model to the desorption branch of the isotherm.

Electron paramagnetic resonance (EPR) experiments were conducted using an X-band (9 GHz) Bruker Elexys E-500 spectrometer (Bruker BioSpin GmbH, Rheinstetten, Germany) that was equipped with a super-high-sensitivity probe head. Solid samples were transferred to flame-sealed glass capillaries that, in turn, were coaxially inserted into a standard 4 mm quartz sample tube. Measurements were conducted at room temperature using the following instrumental settings: 100 G as the sweep width; 1024 points as the resolution; 100 kHz as the modulation frequency; and 1.0 G as the modulation amplitude. The amplitude of the field modulation was preventively determined to be sufficiently low to avoid detectable signal overmodulation. Two sets of EPR measurements were conducted: i. on nanohybrid powder to monitor the organic HA-NDL component and ii. in aqueous suspensions using the spin-trapping method to detect ROS production by TiO_2/HA-NDL nanohybrids. EPR spectra of solid samples were registered with a microwave power of 0.06 mW to

avoid microwave saturation of the resonance absorption curve, and 16 scans were accumulated to improve the signal-to-noise ratio. Power saturation curves were also recorded by varying the microwave power from 0.004 mW to 128 mW. A quantitative analysis (*g*-factor and spin-density values) of the EPR spectra was conducted using an internal standard that was composed of a mixed Mn^{2+}/MgO powder that was inserted in the quartz tube coaxially with the analysed samples. To detect the ROS production by TiO_2/HA-NDL nanohybrids in aqueous dispersions, samples were prepared via the following procedure: A suitable amount of a stock aqueous solution of 5,5-dimethyl-1-pyrroline-1-oxide (DMPO) spin-trap was added to 1 mL of each nanohybrid suspension (2 mg mL^{-1}) to obtain a final spin-trap concentration of 20 mM. After 10 min of dispersion preparation, each suspension was centrifuged at 3000 rpm for 5 min with a mini-centrifuge, and the supernatants were analysed via EPR. The spectra were registered with an attenuation of 15 dB, and 128 scans were accumulated.

DLS measurements were conducted to measure the size with a homemade instrument that was composed of a Photocor compact goniometer, an SMD 6000 Laser Quantum 50 mW light source that operated at 5325 Å, a photomultiplier (PMT-120-OP/B) and a correlator (Flex02-01D) from *Correlator.com*. The experiments were conducted at a constant temperature (25.0 ± 0.1) °C by using a thermostatic bath and at a scattering angle θ of 90°. The scattered intensity correlation function was analysed using a regularization algorithm (Lomakin et al., 2005). The diffusion coefficient of each population of diffusing particles was calculated as the z-average of the diffusion coefficients of the corresponding distributions (Zhang et al., 2008).

SANS measurements were performed at 25 °C with a KWS-2 diffractometer that was operated by the Julich Centre for Neutron Science at the FRMII source at the Heinz-Maier Leibnitz Zentrum (MLZ, Garching, Germany). For all samples, neutrons with a wavelength of 5 Å and $\Delta\lambda/\lambda \leq 0.2$ were used. A two-dimensional array detector at three wavelength (W)/collimation (C)/sample-to-detector (D) distance combinations (W 5Å/C 8 m/D 2 m, W 5Å/C 8 m/D 8 m, and W 5Å/C 20 m/D 20 m) was used to measure neutron scattering from the samples. The scattering intensity *I(q)* was measured in

the range of the modulus of the scattering vector $q = 4\pi n \sin(\theta/2)/\lambda$, between 0.002 $Å^{-1}$ and 0.4 $Å^{-1}$. Here, λ and θ represent the wavelength of the neutron beam and the scattering angle, respectively. The raw experimental data were corrected for background and empty cell scattering after acquisition. Then, the experimental data were fitted with a suitable model by using the SASview program (SASview 4.0.1 software, https://www.sasview.org/) to obtain structural information from the form factor.

2.3 Multifunctional activity of the TiO_2/HA-NDL nanohybrids

2.3.1. Antibacterial assay

An antibacterial activity of the TiO_2/HA-NDL nanohybrids was conducted on various gram-negative and gram-positive bacterial strains, which included *Escherichia coli* DH5a, *Escherichia coli* ATCC 35218, *Klebisella pneumoniae* ATCC 700503, *Pseudomonas aeruginosa* ATCC 27355, *Enterococcus faecalis* ATCC 29212 and *Staphylococcus aureus* ATCC 5538P, which were kindly provided by the Department of Biology of the University of Naples Federico II. Antibacterial activity assays were conducted via the plate viable-count method (Vitiello et al., 2017; Zanfardino et al., 2010). A single colony of each bacterial strain was suspended in 5 mL of Luria-Bertani (LB) broth medium (Becton, Dickinson) and incubated overnight at 37 °C. When the cell cultures reached an OD600 nm of 1 unit, they were diluted with a ratio of 1:100 in 20 mM sodium phosphate buffer (NaP) with pH 7.0. Then, 40 µL of the diluted bacterial cell suspension was alternatively added to the nanoparticle suspensions at various concentrations (10, 25, 50, 100, 200 and 1000 $\mu g \cdot mL^{-1}$) to a final volume of 500 µL using 20 mM NaP buffer with pH 7.0. Cells that were incubated with the ampicillin antibiotic (0.05 mg mL^{-1}) were used as a positive control, whereas cells that were incubated without any compound or with bovine serum albumin (BSA) at the same concentration of the nanoparticles were used as negative controls. The samples were incubated at 37 °C for 4 hours, and their dilutions (1:100 and 1:1000) were placed on an LB/agar medium and incubated overnight at 37 °C. This procedure was also conducted to analyse the antibacterial activity of bare HA-NDL, which was used

as a reference. The following day, the number of surviving cells was estimated by counting the colonies on each plate, and they were compared with the controls. All samples were tested in triplicate, and their means were compared by applying one-way analysis of variance (ANOVA) and Tukey´s HSD test. The statistical analysis was conducted by using XLSTAT software, and significant difference was set at 95% confidence.

2.3.2 Antibiotic removal tests

Amoxicillin, tetracycline and metronidazole were selected for removal tests by TiO_2/HA-NDL nanohybrids due to their presence in wastewater as representatives of the most commonly used antibiotics (Fig. 1). Three independent aqueous antibiotic solutions were prepared at a concentration of 0.50 $mg \cdot mL^{-1}$. Then, 200 μL of each antibiotic solution was added to 800 μL of each TiO_2/HA-NDL suspension to obtain antibiotic and nanoparticle concentrations of 0.1 $mg \cdot mL^{-1}$ and 1 $mg \cdot mL^{-1}$, respectively, in the final mixture.

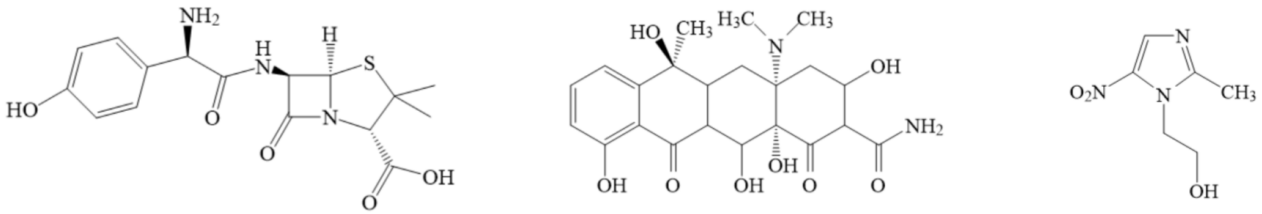

amoxicillin **tetracycline** **metronidazole**

Fig. 1. Molecular structures of the antibiotics that were utilized (by ChemDraw Ultra, version 12.0.2.1076).

After mixing, each obtained suspension was gently stirred on a Roller Mixer SRT2 (Stuart Scientific) for 24 h at 33 rpm and subsequently centrifuged for 20 min at 12000 rpm to induce the precipitation of TiO_2/HA-NDL. All supernatants were recuperated and analysed using a 1100 Agilent (Shimadzu Corp., Japan) high-performance liquid chromatography (HPLC) system that was equipped with a Gemini C18 110A column. The mobile phase was composed of 90% aqueous buffer (MeOH 5% v/v, H_3PO_4 1% v/v) and 10% acetonitrile that was flowing at 1.0 $mL \cdot min^{-1}$. Signals were acquired at 220

and 230 nm for amoxicillin, at 270 and 280 nm for tetracycline and at 320 nm for metronidazole. The retention times were 3.39 and 6.50 min for amoxicillin and tetracycline, respectively. Finally, the chromatograms were integrated using the LC Solution software (Shimadzu Corp., Japan).

3. Results and Discussion

3.1. Physicochemical features of the TiO_2/HA-NDL nanohybrids

The formation of hybrid nanomaterials was verified by evaluating the presence of both inorganic and organic components. XRD patterns of the TiO_2/HA-NDL nanohybrids primarily provided information about the properties of titanium dioxide. For all nanohybrids, the diffraction patterns showed the typical profile of a standard anatase lattice (JCPDS 84-1286) in terms of both peak positions (diffraction angles 2θ) and relative intensities, as demonstrated by comparison with the pure anatase TiO_2 XRD pattern (Fig. 2A) (JCPDS, International Centre for Diffraction Data, 1998). In contrast, HA-NDL was amorphous, and its partial contribution was detected by the presence of a broad halo around the most intense peak in the XRD profile of each TiO_2/HA-NDL nanohybrid. These results demonstrated the formation of crystallized TiO_2 with a mean crystalline size of approximately 6 nm in all samples, as determined by the Scherrer equation; thus, during the hydrothermal treatment, the growth of TiO_2 was not hindered by the addition of HAs. Subsequently, a TG analysis was conducted to assess the organic component amount within the samples. The TG curves of the nanohybrids showed a weight loss in the range of 250-400 °C, which corresponded to the main decomposition of HA according to the TG curve of bare HA (as reported in Fig. S1A). This supported the presence of HAs, and their final content in the samples was measured in the range of 3.5 to 6.0 wt.% and depended on the HA amount that was used during the synthesis. These small changes among the samples could be due both to the presence of a saturated amount of HA that was conjugated with TiO_2 (TiO_2/HA-NDL2 sample) and to the simultaneous presence of triethylamine, which was used as a capping agent, on the TiO_2 surface during hydrothermal synthesis, as demonstrated by the weight loss in the TG curve of the bare TiO_2 nanostructures.

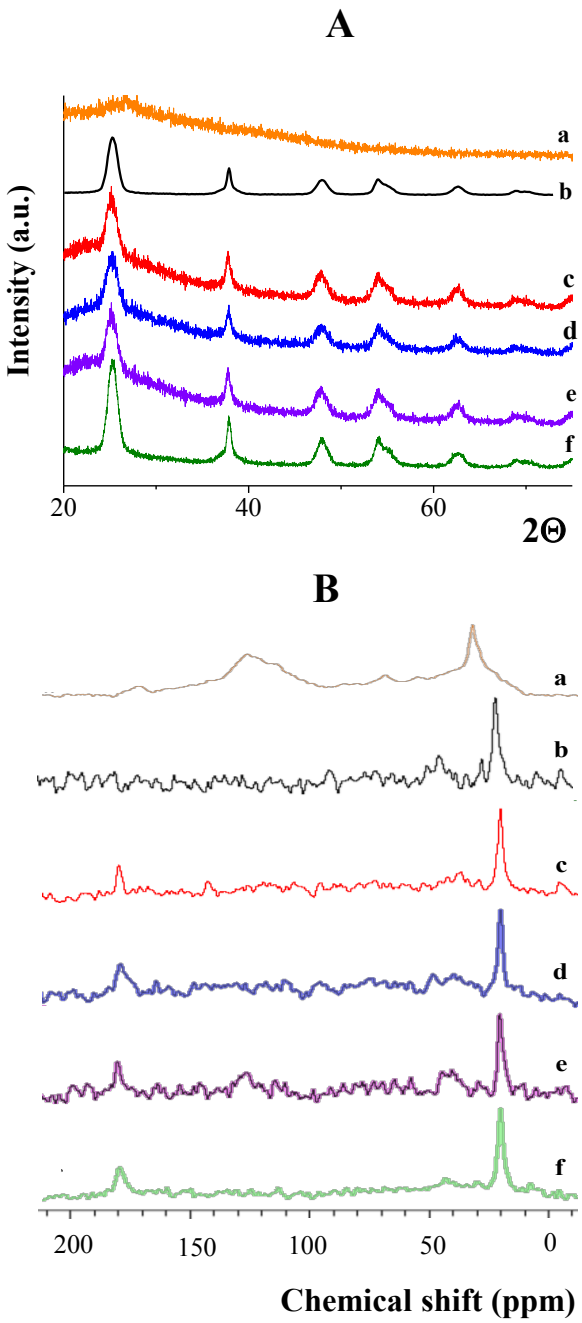

Fig. 2. XRD spectra (**Panel A**) and ^{13}C-cross polarization magic angle spinning NMR spectra (**Panel B**) of pure HA-NDL (**a**), bare TiO_2 (**b**), and TiO_2/HA-NDL_0.1 (**c**), TiO_2/HA-NDL_0.2 (**d**), TiO_2/HA-NDL_1 (**e**), and TiO_2/HA-NDL_2 (**f**) nanohybrids.

The conjugation of HA-NDL with TiO_2 within the hybrid materials is also supported by FTIR and solid-state NMR analyses. The FTIR spectra of TiO_2/HA-NDL showed a typical band in the 3700-3000 cm^{-1} region, which is typical of -OH stretching vibrations. The bands in the range of 2800 to 3000 cm^{-1} were attributed to C-H symmetric and asymmetric stretching vibrations of alkyl groups. The bands in the region 1580-1760 cm^{-1} could be related to C=C bonds in aromatics and olefins, to

carboxyl C=O bonds, and to ketone and quinone moieties (Fig. S1B, Table S1). A band at approximately 1400 cm^{-1} was attributed to phenol -OH, COO- and CH_3 bending vibration modes (Fig. S1 and Table S1) according to previous results (Pota et al., 2020). Another band can be distinguished in the range of 1280-1020 cm^{-1}, which corresponds to the stretching vibration modes of phenolic C-O and aliphatic OH. Indeed, stretching of phosphate groups (PO_4) could contribute to this band; this is supported by the presence of a sharp band at 620 cm^{-1}, which was assigned to PO_4 bending. Typical bands of HAs were distinguished in the FTIR spectra of hybrid TiO_2/HA-NDL nanostructures (Fig. S1), which were similar to the bands in the FTIR spectrum of bare HA-NDL, thereby supporting the presence of HAs in the samples. These bands appear at higher frequency in comparison to the FTIR spectrum of bare HA, which may be due to the increase in the force constant that was caused by complexation with Ti(IV) ions (Guan et al., 2007). Moreover, the FTIR spectra of both bare TiO_2 and the TiO_2/HA-NDL nanostructures showed a clear band at 1621 cm^{-1}, which can be assigned to the N–H bending vibration of the primary amine, thereby suggesting the presence of residual triethylamine (Fig. S1B).

^{13}C-CPMAS spectra that were acquired for TiO_2/HA-NDL samples were compared with spectra for the bare HA-NDL and TiO_2. As shown in Fig. 2B, the HA-NDL NMR spectrum was principally characterized by three resonance regions (spectrum a) that were centred at i. ~170 ppm, which is typical of the carboxyl groups; ii. ~130 ppm, which was attributed to aromatic moieties, and iii. ~30 ppm, which was attributed to alkyl carbons. In the TiO_2/HA-NDL spectra (Fig. 2B, c-f), the presence of humic acid was mainly proven by the appearance of the carboxyl group signal and, to a lesser extent, by aromatic carbon resonance. The additional signal in the 10-30 ppm range was ascribed to triethylamine that remained partially adsorbed on the surface of the hybrid nanostructures, which was also observed in the bare TiO_2 spectrum b of Fig. 2B. In contrast, the ^{13}C-CPMAS and ^{1}H BBI spectra revealed that no significant change in the HA fraction by the hydrothermal treatment (Fig. S2). Therefore, NMR spectroscopy indicated the conjugation of titanium dioxide with humic acid.

A morphological analysis of the TiO_2/HA-NDL samples was conducted via TEM. As shown in Fig. 3A-B, the TEM images indicated the formation of small nanoparticles of ~20 nm in size with a rod-like structure. These TiO_2/HA-NDL nanoparticles appeared slightly smaller than the bare TiO_2 nanoparticles (~30-35 nm), which were prepared via the same synthesis route in the absence of HAs, as shown in Fig. 3C-D, and according to our previous studies (Vitiello et al., 2015; Vitiello et al., 2017). However, the presence of HA-NDL during TiO_2 growth seems to modulate the hierarchical organization of the TiO_2/HA-NDL nanoparticles. This led to disordered hybrid clusters with an average size of ~200 nm (Fig. 3A) in comparison to the larger irregular aggregates that were obtained for the bare TiO_2 sample (Fig. 3C). This difference can be ascribed to the close interconnection at the molecular scale between the two components, in which TiO_2 nanoclusters/primary particles were likely held together by the HA-NDL molecules.

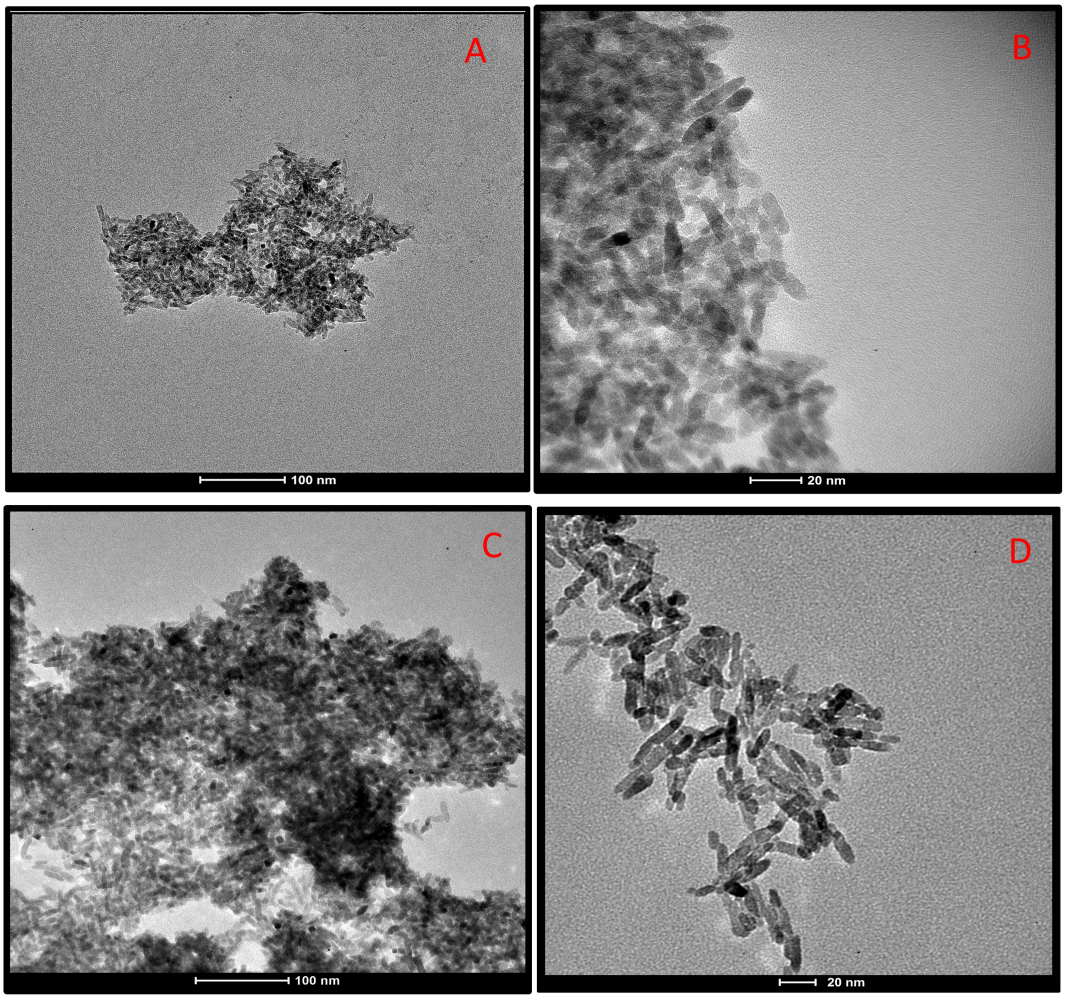

Fig. 3. TEM images of hybrid TiO_2/HA-NDL (**A**, **B**) in comparison with bare TiO_2 (**C**,**D**) nanostructures.

Subsequently, the surface properties of the TiO_2/HA-NDL hybrids were investigated by obtaining N_2 adsorption isotherms, as shown in Fig. 4A. They were classified as Type IVb, which is typical of mesoporous materials that show capillary condensation that is accompanied by hysteresis on the desorption branch (Venezia et al., 2020). The values of the specific surface area (BET method) and total pore volume for each sample are reported in Table 2. The specific surface area of the reference TiO_2 sample was 169 $m^2 g^{-1}$ according to previous evidence (Vitiello et al., 2015; Vitiello et al., 2017), while all samples that were prepared via HA-NDL addition showed larger values, which reached a maximum of approximately 240 $m^2 g^{-1}$ for samples with intermediate HA-NDL contents (TiO_2/HA-NDL_0.2 and TiO_2/HA-NDL_1). The slight decrease in the surface area of the TiO_2/HA-NDL_2 sample with respect to the others could be explained by the addition of a larger amount of organic matter in the reaction solution, which created a larger fraction of HA moieties on the surfaces of the primary colloidal TiO_2 nanoparticles. This caused an increase in the number of negative surface charges, thereby limiting the particle assembly and influencing the growth of hybrid materials, which were therefore characterized by a smaller surface area (Pota et al., 2020). In addition, as presented in Table 2, the changes in the surface areas of the hybrid materials with respect to that of bare TiO_2 nanoparticles were accompanied by a slight decrease in the total pore volume of the samples. The HA-NDL organic component on its own was characterized by a small specific surface area and a small pore volume. The pore size distribution analysis in Fig. 4B clearly shows that HA-NDL addition caused a significant decrease (~20 Å) in the average diameter of the mesopores.

A narrow, monomodal pore size distribution that extended from 20 to 60 Å with a sharp maximum centred at ~45 Å was exhibited by all TiO_2/HA-NDL samples, in contrast to the broader distribution of the reference TiO_2 sample, which extended from 20 Å up to 100 Å and had a smaller peak at ~70 Å. This result seems to support the key role of HAs in modulating the growth and the consequent structural organization of TiO_2-based hybrid nanostructures by modifying their final surface area and porosity.

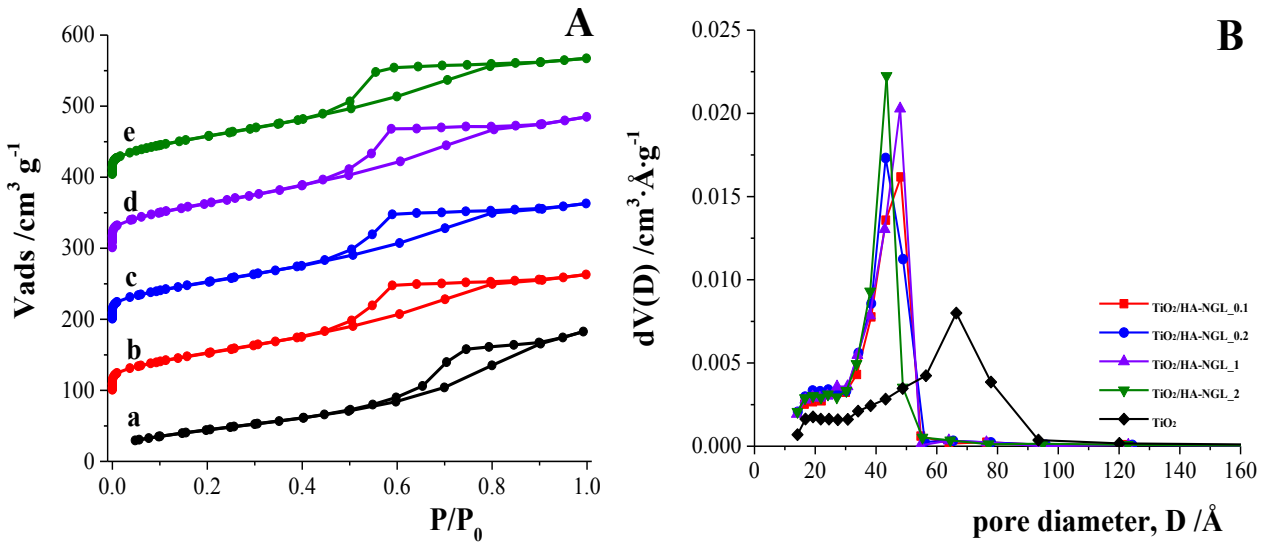

Fig. 4. N_2 adsorption isotherms at 77 K (panel **A**) that correspond to TiO_2 (**a**), TiO_2/HA-NDL_0.1 (**b**), TiO_2/HA-NDL_0.2 (**c**), TiO_2/HA-NDL_1 (**d**) and TiO_2/HA-NDL_2 (**e**) and BJH pore distribution curves (panel **B**) for bare TiO_2 and TiO_2/HA-NDL nanohybrids at various compositions.

Table 2 - Surface area and pore properties of HA-NDL, TiO_2 and hybrid TiO_2/HA-NDL nanostructures.

Sample	Surface area (m^2/g) (± 7%)	Pore volume (cm^3/g) (± 0.02)	Average pore diameter (Å) (± 10%)
HA-NDL	15	0.02	-
TiO_2	169	0.30	66
TiO_2/HA-NDL_0.1	210	0.25	48
TiO_2/HA-NDL_0.2	240	0.27	43
TiO_2/HA-NDL_1	244	0.29	48
TiO_2/HA-NDL_2	227	0.26	43

Exploiting the intrinsic paramagnetic properties of HA components, EPR measurements were also conducted on the TiO_2/HA-NDL samples by following an experimental approach that was already tested for the characterization of polyphenols and/or melanin-like materials (Cesareo et al., 2012; Panzella et al., 2018; Vitiello et al., 2015; Vitiello et al., 2017). The analysis of the EPR signal provides significant information regarding the characteristics of the paramagnetic centres and the supramolecular properties of the organic moieties that constitute the TiO_2/HA-NDL nanohybrids.

A similar line shape was observed for all EPR spectra in Fig. 5A, namely, a single, roughly symmetric signal at a *g* value of 2.0031 ± 0.0003, which is typical of carbon-centred radicals of HAs and similar

polyaromatic molecules (Jezierski et al., 2000; Panzella et al., 2018), with a spin-density concentration that depends on the amount of HA-NDL that was used during the synthesis (Table 3). Upon closer inspection of the spectra, no differences in the spectral line shape among the TiO_2/HA-NDL samples were observed, and the line shape was highly similar to that of pure HA-NDL. This finding was supported by the quantitative determination of the signal amplitude, ΔB, which is related to the linewidth of the EPR peak, as detected from the experimental spectra (as shown in Fig. 5A). Typically, the linewidth of an EPR peak depends on the relaxation time of spinning electrons and is affected mainly by the unresolved hyperfine interactions between unpaired electrons and neighbouring atoms (Buszman et al., 2006). A broad line shape is due to the superposition of multiple signals that are associated with the presence of various carbon-based paramagnetic species. The narrowing of the line shape is related to the presence of stronger electron-electron interactions and can be associated with a more locally ordered organization of the polyaromatic structures that host the unpaired electrons. Hence, this parameter is usually considered indicative of the mean distance between the radical centres.

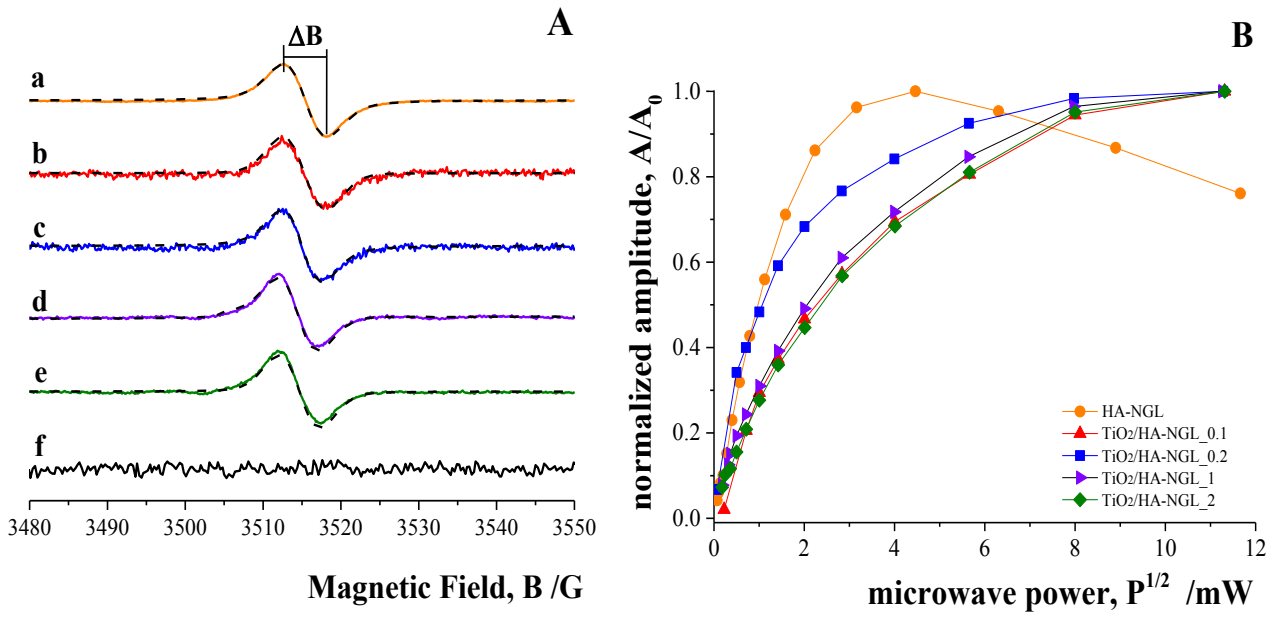

Fig. 5. EPR spectra (**panel A**) and power saturation curves that were obtained by plotting the normalized amplitude (A/A_0) values *versus* the square roots of microwave power intensities (P) of free radicals (**panel B**) in HA-NDL powder (**a** and ●) and TiO_2/HA-NDL_0.1 (**b,** ▲), TiO_2/HA-NDL_0.2 (**c,** ■), TiO_2/HA-NDL_1 (**d,** ►) and TiO_2/HA-NDL_2 (**e,** ♦) nanostructures. The flat EPR spectrum of bare TiO_2 is reported for reference (**f**).

As reported in Table 3, the determined ΔB values are 5.6 ± 0.2 G for all samples; thus, the structural organization of the organic moiety was not perturbed in the nanohybrids. This value was also obtained for bare HA-NDL after hydrothermal treatment in the absence of an inorganic phase, as reported in Fig. S3. Then, EPR spectra of each sample were recorded by increasing the incident microwave power. The power saturation curves were obtained by plotting the normalized peak amplitude (A/A_0) as a function of the square root of the microwave power (P), as shown in Fig. 5B. A non-monotonic trend with a decrease in amplitude for microwave powers, $P^{1/2}$, of higher than 4 mW was observed for bare HA-NDL; thus, free radicals presented long relaxation times and were homogeneously located in the sample. In contrast, a monotonic increase was observed for TiO_2/HA-NDL systems; hence, all free radical spins did not exhibit the same relaxation behaviour and saturated independently. This result demonstrates that the radical centres present a chemically inhomogeneous distribution, which is likely associated with the presence of aromatic moieties that were conjugated with Ti(IV) ions on which the unpaired electrons were stabilized. This suggests possible chemical changes due to the combination with the inorganic component during nanohybrid synthesis. The occurrence of this phenomenon was also supported by the Lorentzian (and Gaussian) contribution in the line shape of the recorded spectra, which was estimated by determining the best fitting curves of each EPR signal and using them to analytically discriminate the relative contributions. An increase in the Gaussian character of the EPR signals for all TiO_2/HA-NDL nanohybrids was observed, which supports the presence of more radical centres than in HA-NDL with relaxation behaviours that differ from that in HA-NDL (Table 3).

In consideration of these paramagnetic properties of the TiO_2/HA-NDL hybrid nanostructures, their ability to generate ROSs in aqueous environments was investigated via the EPR spin-trapping method. This is a useful method for detecting the formation of radical species with extremely high chemical reactivity, which typically have lifespans that are too short for direct detection (Davies et al., 2016; Villamena et al., 2004). These reactive free radicals are put in contact with a suitable amount of a DMPO spin-trap to extend the lifetimes of their spin-adducts, which can be monitored via EPR

spectroscopy at room temperature. Following this approach, an initial analysis was conducted to preventively verify that DMPO in an aqueous environment did not produce any interfering signal (Fig. 6a). Then, an EPR signal that was constituted by a quartet with a 1:2:2:1 intensity ratio (Fig. 6b) was detected for the supernatants of all nanohybrid suspensions, which corresponded to the DMPO-OH adduct that formed from the trapping of •OH radicals by the DMPO molecule. This finding was supported by the quantitative analysis results of the spectrum, according to which the hyperfine coupling constants for the nitroxide nitrogen and for the β-proton were $a_N = a^{\beta}_H = 14.8 \pm 0.2$ G. These values are consistent with those reported in the literature for the DMPO-OH adducts (Dvoranová et al., 2014; Pirozzi et al., 2020), thereby supporting the formation of •OH radical species. No significant differences were detected in the EPR spectra that corresponded to the TiO_2/HA-NDL nanohybrids, and no signal of DMPO- adducts was appreciated in the spectra of neat TiO_2 or HA-NDL. This result suggests that the synergistic combination of HA-NDL and TiO_2 within hybrid nanostructures plays a key role in the ROS-generating ability of the final nanohybrids. HAs undergo reversible redox reactions, and under aerated conditions, semiquinone moieties are further oxidized, which causes electron transfer to O_2 and, ultimately, the formation of •OH radicals (Pirozzi et al., 2020; Vitiello G. et al., 2018). This process could be more significant in TiO_2/HA-NDL nanostructures, which have larger exposed surface areas than bare HA-NDL. In addition, it can be assumed that catechol moieties within the HA backbone can act as ligands for Ti^{4+} ions, thereby forming a ligand-to-metal charge transfer complex (LMCTC), which could cause ROS production by the TiO_2 component in hybrid nanostructures, even upon visible light irradiation (Vitiello G. et al., 2016). This evidence underlines the key role of the molecular combination of the organic and inorganic components in improving the capability of the hybrid nanomaterials to generate radical species, in contrast to the behaviour that is exhibited by the commonly designed humic acid-coated TiO_2 nanoparticles (Lin D. et al. 2012; He X. et al. 2016), which showed a drastic decrease in the ability of TiO_2 to produce •OH or $•O_2^-$ radicals, thereby limiting their use in ROS-mediated applications (antimicrobial agents).

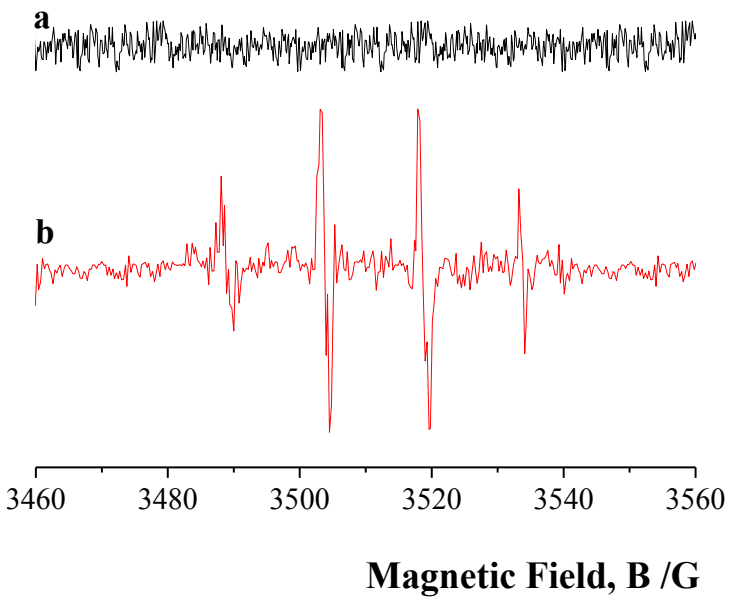

Fig. 6. EPR spectra of a DMPO aqueous solution (**a**) and in the presence of TiO_2/HA-NDL hybrid nanostructures (**b**) without light irradiation.

Table 3 – EPR spectral parameters and structural values that were obtained from the best fits of SANS curves for the obtained TiO_2/HA-NDL hybrid nanostructures. The estimated experimental uncertainties are ± 0.0003 for the g-factor, ± 0.2 G for ΔB and ± 10% for the spin-density.

Sample	g-factor	ΔB/G	Lorentzian %	spin × g^{-1} × 10^{16}	R_a (nm)	R_b (nm)
HA-NDL	2.0031	5.6	35%	5.80	-	-
TiO_2/HA-NDL_0.1	2.0032	5.6	15%	0.19	-	-
TiO_2/HA-NDL_0.2	2.0031	5.5	20%	0.50	21 ± 1	115 ± 2
TiO_2/HA-NDL_1	2.0031	5.6	23%	0.88	15 ± 2	111 ± 6
TiO_2/HA-NDL_2	2.0032	5.5	20%	1.70	19 ± 4	116 ± 3

DLS and SANS experiments were conducted to evaluate the colloidal stability and the self-assembly behaviour of the TiO_2/HA-NDL nanohybrids in aqueous environments. DLS measurements provide information about the sizes of the hybrid nanostructures. Since all suspensions were dilute, the Stokes–Einstein equation was used to evaluate the hydrodynamic radius, R_H, of the aggregates from their translation diffusion coefficient, D:

$$r_H = \frac{kT}{6\pi\eta_0 D} \quad (1)$$

where k is the Boltzmann constant, T is the absolute temperature and $\eta_0=0.89\ cP$ is the solvent viscosity. For non-spherical particles, r_H represents the radius of a spherical aggregate with the same diffusion coefficient (Benoit, 1997; Pecora, 2003; Roscigno et al., 2001; Luchini et al., 2016). As shown in Fig. 7A, a monomodal distribution curves for all samples were obtained via DLS analysis, which suggest the presence of a single population of hybrid nanostructures in an aqueous environment with a mean r_H of between 80-85 ± 5 nm and a polydispersity index of approximately 0.5. In contrast, a larger average hydrodynamic radius (150 ± 5 nm) was observed for the sample that was prepared in the presence of the lowest HA-NDL amount, namely, TiO_2/HA-NDL_0.1, which suggests that the use of a small amount of the organic component during the synthesis favoured the formation of larger nanostructures. Moreover, this sample was not highly stable in the aqueous medium, and it exhibited fast aggregation and precipitation. These results demonstrate the key role of HAs in modulating the agglomeration process of TiO_2 nanostructures, which is directly related to the presence of aromatic moieties in the HA matrix, thereby leading to a stronger stabilization effect (Zhao et al., 2019).

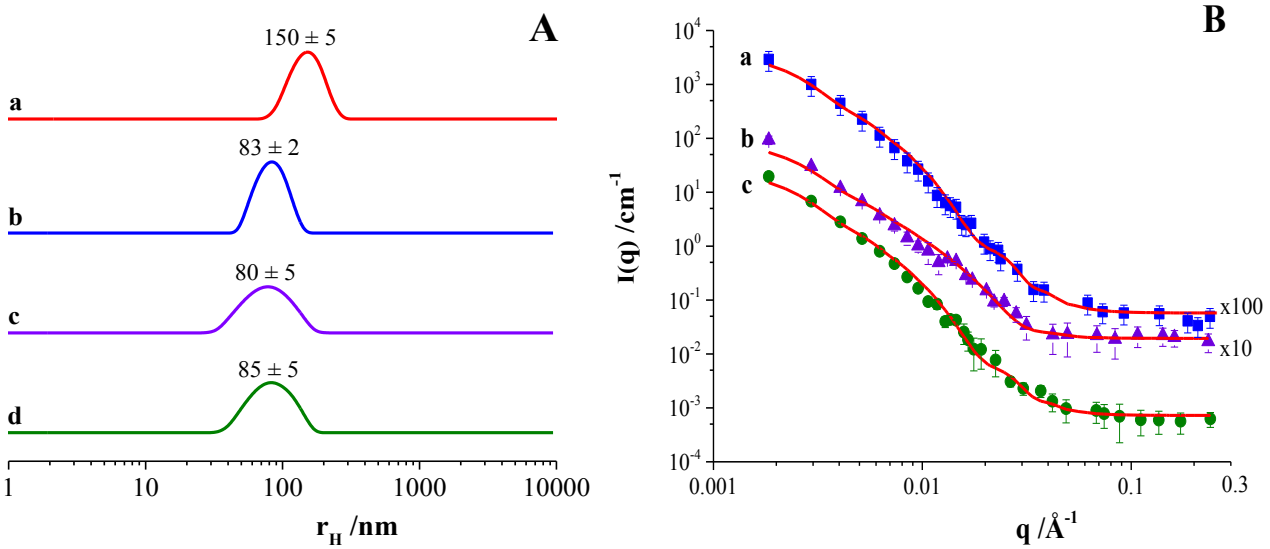

Fig. 7. **Panel A**: Hydrodynamic radius distribution functions that were obtained at 25 °C and 90° via DLS measurements for hybrid TiO_2/HA-NDL nanostructures that were prepared with various HA-NDL/titanium isopropoxide molar ratios: TiO_2/HA-NDL_0.1 (**a**), TiO_2/HA-NDL_0.2 (**b**), TiO_2/HA-NDL_1 (**c**) and TiO_2/HA-NDL_2 (**d**). **Panel B:** SANS profiles and the corresponding best fitting curves of hybrid TiO_2/HA-NDL_0.2 (**a**), TiO_2/HA-NDL_1 (**b**) and TiO_2/HA-NDL_2 (**c**) suspensions in D_2O. Profiles (**a**) and (**b**) are offset for clarity.

SANS measurements were conducted to investigate the structural properties of the TiO_2/HA-NDL nanostructures and their hierarchical organization at 25 °C. All suspensions were prepared in D_2O to exploit the difference in scattering length density, ρ, between the solvent ($\rho_{D_2O} = 6.34 \times 10^{-6}$ Å^{-2}) and the nanostructures ($\rho_{TiO_2} = 2.44 \times 10^{-6}$ Å^{-2}; 1.4×10^{-6} Å$^{-2} < \rho_{humic-acids} < 2.2 \times 10^{-6}$ Å^{-2}) (Jarvie et al., 2007; Wenk, 2018). The collected experimental data are reported in Fig. 7B, together with the corresponding fitting curves for all systems except the TiO_2/HA-NDL_0.1 sample, for which a SANS measurement was not acquired due to the instability and fast precipitation of these nanoparticles. The quantitative analysis of SANS data required the identification of a suitable model to describe the scattered intensity vs q for the extraction of structural information about the sample. The scattering intensity values, $I(q)$, vs q for all aqueous dispersions of hybrid TiO_2/HA-NDL nanostructures are presented in Fig. 7B.

Accordingly, due to the similar scattering length densities of the inorganic and organic components, all hybrid samples were modelled as collections of ellipsoids with an inner core and an outer shell that have the same scattering length densities. The theoretical expression of $I(q)$ for oriented ellipsoids was defined by Feigin, in which the form factor for an ellipsoid with uniform scattering length density is normalized by the particle volume (Feigin et al., 1987):

$$I(q) = \frac{k}{V_P} f^2(q) + bkg \tag{2}$$

where:

$$f(q) = \frac{3(\Delta\rho)V_P(\sin[qr(R_a, R_b)] - qr\cos[qr(R_a, R_b)]}{[qr(R_a, R_b)]^3} \tag{3}$$

and

$$r(R_a, R_b) = [R_b^2 + R_a^2]^{1/2} \tag{4}$$

in which k denotes the volume fraction of the particles, V_P is the volume of the ellipsoid, R_a is the radius along the rotational axis of the ellipsoid, R_b is the radius perpendicular to the rotational axis of the ellipsoid and $\Delta\rho$ is the difference in scattering length density between the scatterer systems and

the solvent. The optimal values of these parameters were obtained via data fitting and are collected in Table 4. The SANS analysis results demonstrated the formation of ellipsoid nanostructures in which small TiO_2 nanoparticles were randomly assembled with the organic component, which is supported by the experimental ρ value (~2.0×10^{-6} Å^{-2}) of the nanostructures that was determined via the fitting procedure, which is between the calculated ρ values of TiO_2 and Has, as expected. The fit also indicated that no significant changes in R_a and R_b were induced by increasing the amount of HA during synthesis (Table 3), thereby demonstrating a similar structural organization of all nanohybrids, which is in agreement with the DLS and TEM results. However, for TEM, the solvent evaporation that was required for sample preparation was expected to promote the clustering of hybrid nanoparticles. This could lead to changes in the morphology of the hybrid clusters with respect to the morphology that was observed in solution.

3.2. Multifunctional activity of the TiO_2/HA-NDL nanohybrids

3.2.1 Antibacterial properties

The antibacterial activity of the TiO_2/HA-NDL nanostructures was evaluated using four strains of gram-negative bacteria (*E. coli DH5a, E. coli* ATCC35218*, K. pneumonia* and *P. aeruginosa*) and two strains of gram-positive bacteria (*E. faecalis* and *S. aureus*). These strains were chosen due to their high diffusion in water and healthcare environments and their ability to develop strong resistance to common antibiotics. The experimental results are reported in Fig. 8. First, the bare TiO_2 nanostructures are not active against all the bacterial strains (as reported in Fig. S4).

The TiO_2/HA-NDL nanostructures were tested at various concentrations that ranged from 10 to 1000 $\mu g \cdot mL^{-1}$ to evaluate the possible influence of the concentration of the nanosystem on the survival of bacterial strains without irradiation. As shown in Fig. 8, an increasing trend of the antimicrobial activity with the nanoparticle concentration was observed against both *Escherichia coli DH5a* and *Escherichia coli* ATCC 35218. The observed biocide activity as a function of the HA-NDL content differed among the nanohybrids: the TiO_2/HA-NDL_0.1 sample showed satisfactory activity up to

50 μg·mL^{-1}, while the samples (0.2, 1 and 2) that were prepared with higher HA-NDL contents exhibited moderate activity already at the lowest concentration of 10 μg·mL^{-1} up to the maximum of 1000 μg·mL^{-1}.

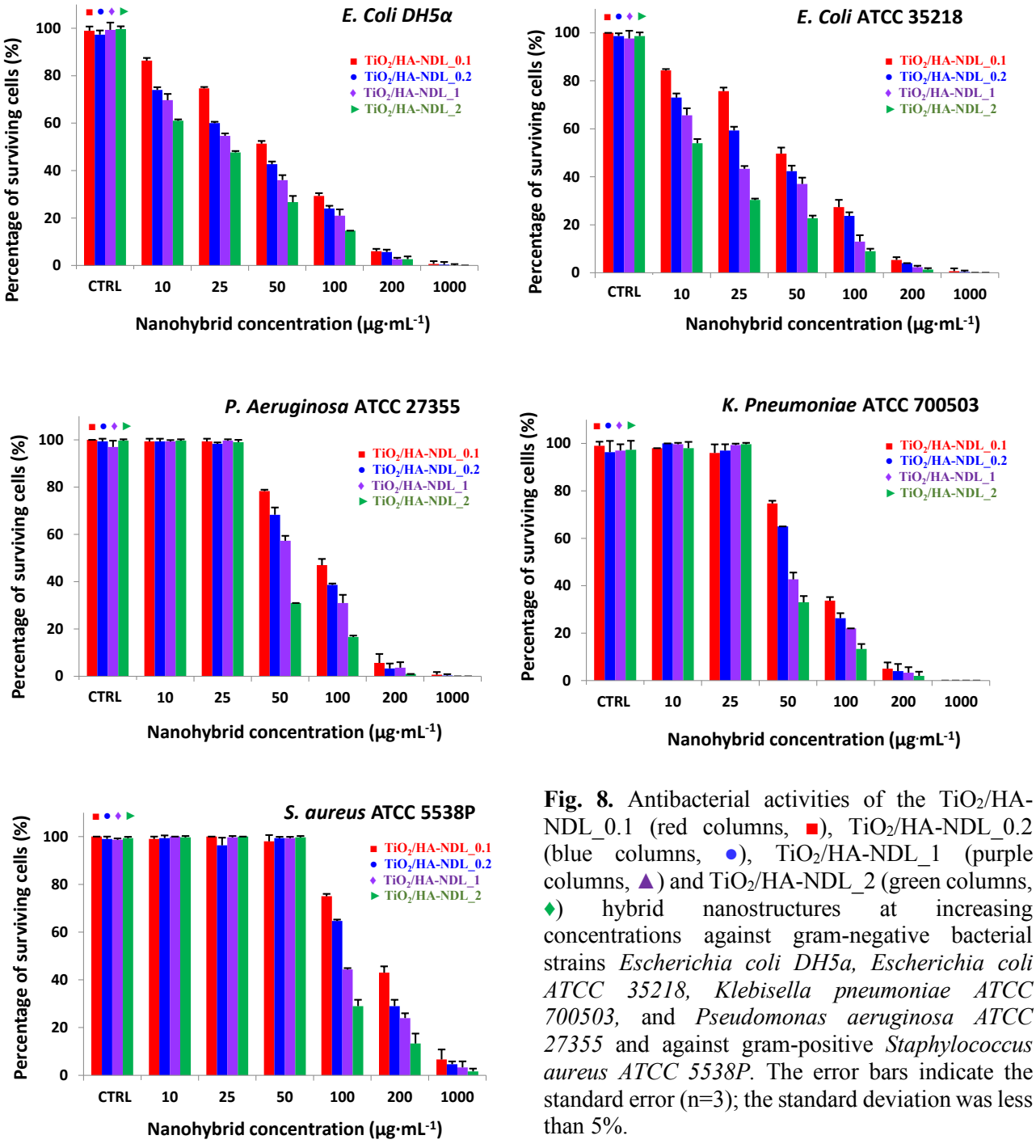

Fig. 8. Antibacterial activities of the TiO_2/HA-NDL_0.1 (red columns, ■), TiO_2/HA-NDL_0.2 (blue columns, ●), TiO_2/HA-NDL_1 (purple columns, ▲) and TiO_2/HA-NDL_2 (green columns, ♦) hybrid nanostructures at increasing concentrations against gram-negative bacterial strains *Escherichia coli DH5a, Escherichia coli ATCC 35218, Klebisella pneumoniae ATCC 700503,* and *Pseudomonas aeruginosa ATCC 27355* and against gram-positive *Staphylococcus aureus ATCC 5538P.* The error bars indicate the standard error (n=3); the standard deviation was less than 5%.

Moreover, our results demonstrate that the best antibacterial performance was realized by the TiO_2/HA-NDL_2 sample, which was prepared with the highest content of HAs at all tested concentrations, except for the 200 and 1000 μg·mL^{-1} samples, for which no significant differences

were identified between TiO_2/HA-NDL_1 and TiO_2/HA-NDL_2. As also shown in Fig. 8, pronounced activity was observed for the TiO_2/HA-NDL samples against the *Pseudomonas aeruginosa ATCC 27355* and *Klebisella pneumoniae ATCC700503* strains of gram-negative bacteria. For these strains, the hybrid nanostructures showed a marked biocidal activity from 50 $\mu g \cdot mL^{-1}$, and in these cases, the biocide activity of the TiO_2/HA-NDL samples increased as a function of the HA-NDL content. Finally, antibacterial activity tests were conducted against the *Staphylococcus aureus* ATCC 5538P and *Enterococcus faecalis* ATCC 29212 strains of gram-positive bacteria. A low activity against *Staphylococcus aureus* ATCC 5538P was observed since the biocide effect of the nanohybrids became observable at a concentration of 100 $\mu g \cdot mL^{-1}$ (Fig. 8). No activity was detected against *Enterococcus faecalis* (data not shown). According to these results, the TiO_2/HA-NDL nanohybrids exhibited lower biocide efficacy against gram-positive bacteria.

The antibacterial results are in accordance with the EPR results, according to which the spin-density values increase with the HA content. This finding supports the hypothesis that the large amount of free electrons that were stabilized in the organic structures that were combined with TiO_2 at the molecular scale were responsible for the generation of •OH in the bacterial cell environment, which is also supported by the results of EPR spin-trapping experiments, thereby producing biocidal activity through ROS-mediated cell damage (Nain et al., 2020; Vitiello et al., 2018). Indeed, HAs have been proven to interact with aquatic bacteria (Tikhonov et al., 2010) to promote ROS action against pathogens.

The antibacterial results that were obtained *in vitro* seem to suggest that the biocidal efficacy of the TiO_2/HA-NDL nanohybrids depended strongly on the HA content (Huang et al., 2020; Rainer et al., 1978; van Rensburg et al., 2000), which directly contributed to the increase in the relative amount of generated •OH species, and on the concentration of nanohybrids that were in contact with the various bacterial cultures. However, the differences in behaviour between the gram-negative and gram-positive strains towards nanostructured materials are most likely due to the differences in composition and structural organization of the external bacterial membranes. This experimental evidence supports

the hypothesis of a synergistic role of the inorganic and organic components in determining the antibacterial activity of humic acid-based materials, even under visible light irradiation. Indeed, it is demonstrated that humic substances can promote bacterial growth (Tikhonov et al., 2010), and other studies have demonstrated high efficacies of humic materials, such as oxifulvic and humic acids, against microbial pathogens (van Rensburg et al., 2000), for example, by hindering the growth of *Staphylococcus aureus* and *Candida albicans* or decreasing the number of colonies in *Escherichia coli* and *Salmonella enteritidis* (Yarkova et al., 2011). Consequently, the antibacterial activity of HAs is related to the extraction method and to the molecular composition of the humic acid, which depends on the natural source from which it was obtained (Nebbioso and Piccolo, 2013). Therefore, the combination of these highly reactive substances with an inorganic phase provides a chemical strategy for modulating their chemical functionalities to obtain alternative bioinspired materials with enhanced biocide activity.

3.2.2. Antibiotic sequestering activity

The capability of TiO_2/HA-NDL hybrid nanostructures to sequester the three antibiotics, namely, amoxicillin, tetracycline and metronidazole, was investigated by conducting HPLC analysis on the supernatants. These supernatants were separated via centrifugation from suspensions that contained a mixture of each antibiotic with TiO_2/HA-NDL nanohybrids, as previously described for the adsorption of biomolecules by porous nanomaterials (Califano et al., 2018; Stan et al., 2017). The behaviour of the nanohybrids was also compared with that of bare TiO_2 nanoparticles. It was not possible to monitor the performance of neat HA-NDL in sequestering the three antibiotics because HA-NDL showed a high solubility in the aqueous medium and a very low tendency to precipitate via centrifugation, thereby preventing antibiotic separation from the supernatant. The HPLC analysis showed that metronidazole was not sequestered by the TiO_2/HA-NDL nanohybrids since the antibiotic concentration remained unaffected, which suggests a possible selectivity of these hybrid nanomaterials in antibiotic removal. A similar behaviour was also observed for bare TiO_2. The HPLC

results demonstrate satisfactory sequestering by all nanohybrids of both amoxicillin and tetracycline molecules, and these nanohybrids outperform TiO_2 in sequestering these antibiotics. Small residual amounts were detected in aqueous environments, as reported in Table 4. Increased selectivity towards tetracycline was observed for all TiO_2/HA-NDL nanohybrids, while the best performance in sequestering both antibiotics was detected for the TiO_2/HA-NDL_1 system. Antibiotic removal occurs essentially through an adsorption mechanism that is based on electrostatic interactions and on complex formation with discrete sites in humic acid (Sibley et al., 2008).

Table 4 - Residual percentages of amoxicillin and tetracycline antibiotics that were determined after their contact with TiO_2/HA-NDL hybrid nanostructures in aqueous environments.

Sample	Amoxicillin wt% residue (±5%)	Tetracycline wt% residue (±5%)
TiO_2	28.2	9.6
TiO_2/HA-NDL_0.2	25.4	10.2
TiO_2/HA-NDL_1	8.50	< 5.0
TiO_2/HA-NDL_2	12.7	13.5

Thus, the high activities of the TiO_2/HA-NDL samples towards the removal of antibiotics could be due to the larger surface areas of the nanohybrids compared to that of bare TiO_2 and, concurrently, to the presence of pores in the hydrated hybrid nanostructures with sizes that are compatible with the molecular dimensions of the investigated antibiotics (Fig. 1). Water uptake of HA moieties could play a key role in influencing the organization of their supramolecular structures, which undergo swelling (Kučerík et al., 2011). This phenomenon is expected to produce larger pore sizes that can host organic molecules. Both of these surface features, which are due to the presence of HAs and their combination with the inorganic phase at the molecular scale, induced increased sequestration behaviour in the final hybrid nanosystems. Ultimately, the obtained results agree with recent reports on the application of humic acid-based nanomaterials in the removal of pesticides and antibiotics (Mahmoud et al., 2020; Song et al., 2019; Xu et al., 2019). This opens new opportunities for the development of hybrid

biomass-derived nanomaterials for pharmaceutical removal (Phoon et al., 2020) and, thus, contributes to solving one of the most prominent environmental problems that is faced in public health.

4. Conclusions

This study establishes a synthetic approach that transforms environmental issues that are linked to the interactions of HAs with organic pollutants and inorganic nanoparticles into a technological tool. Hybrid multifunctional humic acid/titanium dioxide nanomaterials have been designed and prepared via solvothermal synthesis, which show substantial promise for environmental applications. The combination at the molecular scale of humic acids from North Dakota leonardite, HA-NDL and the inorganic TiO_2 phase confers high sequestering efficiency towards amoxicillin and tetracycline antibiotics and enhances significant ROS-mediated biocide properties against many pathogenic gram-negative bacteria. Our findings demonstrate the feasibility of the proposed strategy for the design of hybrid nanomaterials with improved and tuneable properties. Moreover, the multiple applications of these nanomaterials offer a versatile approach for usefully employing molecules from either geochemical deposits or recycled biomasses. This strategy provides a technological route to biowaste valorisation and concurrently addresses environmental and health problems that are linked to antibiotic and pathogen water contamination in the furrow of a circular economy to enhance the quality of life.

Conflicts of interest

There are no conflicts of interest to declare.

Acknowledgments

The authors are grateful to Dr. Eugenio Notomista (Department of Biology, University of Naples Federico II) for having supplied bacterial strains and Dr. Rocco Di Girolamo (Department of

Chemical Science, University of Naples Federico II) for his support in TEM analysis. The authors also thank the Heinz-Maier Leibnitz Zentrum (MLZ), for award of beamtime and use of the facility. This work benefited from the use of the SasView application, originally developed under NSF Award DMR-0520547. SasView also contains code developed with funding from the EU Horizon 2020 programme under the SINE2020 project Grant No 654000.

References

Aeschbacher, A., Graf, C., Scwarzenbach, R.P., Sander, M., 2012. Antioxidant properties of humic substances. Environ. Sci. Technol. 46, 4916-4925.

Afzal, M. Z., Yue, R., Sun, X.F., Song, C., Wang, S.G., 2019. Enhanced removal of ciprofloxacin using humic acid modified hydrogel beads. Journal of Colloid and Interface Science 543, 76-83.

Allard, B., Borén, H., Pettersson, C., Zhang, G., 1994. Degradation of humic substances by UV irradiation. Environment International 20, 97-101.

Benoit, J. S. H. H. C., 1997. Polymers and Neutron Scattering, Clarendon Press.

Buszman, E., Pilawa, B., Zdybel, M., Wilczyński, S., Gondzik, A., Witoszyńska, T., Wilczokc, T., 2006. EPR examination of Zn^{2+} and Cu^{2+} binding by pigmented soil fungi *Cladosporium cladosporioides*, Science of The Total Environment 363, 195-205.

Califano, V., Sannino, F., Costantini, A., Avossa, J., Cimino, S., Aronne, A., 2018. Wrinkled silica nanoparticles: efficient matrix for β-glucosidase immobilization. J. Phys. Chem. C 122, 8373-8379.

Cesareo, E., Korkina, L., D'Errico, G., Vitiello, G., Aguzzi, M.S., Passarelli, F., Pedersen, J.Z., Facchiano, A. An Endogenous Electron Spin Resonance (ESR) Signal Discriminates Nevi from Melanomas in Human Specimens: A Step Forward in Its Diagnostic Application. PLoS ONE 7, 2012, e48849.

Cozzolino, A., Piccolo, A., 2002. Polymerization of dissolved humic substances catalyzed by peroxidase. Effects of pH and humic composition. Organic Geochemistry 33, 281-294.

Davies, M.J., 2016. Detection and characterisation of radicals using electron paramagnetic resonance (EPR) spin trapping and related methods. Methods 109, 21-30.

de Melo, B.A.G., Motta, F.L., Santana, M.H.A. Humic acids: Structural properties and multiple functionalities for novel technological developments, 2016. Materials Science and Engineering C 62, 967-974.

de Oliveira, L.K., Molina, E. F., Moura, A.L.A., de Faria, E.H., Ciuffi, K.J., 2016. Synthesis, characterization, and environmental applications of hybrid materials based on humic acid obtained by the sol−gel route. ACS Appl. Mater. Interfaces 8, 1478−1485.

Drosos, M., Nebbioso, A., Mazzei, P., Vinci, G., Spaccini, R., Piccolo, A. 2017. A molecular zoom into soil Humeome by a direct sequential chemical fractionation of soil. Science of the Total Environment 586, 807-816.

Du, Q., Li, G., Zhang, S., Song, J., Zhao, Y., Yang, F., 2020. High-dispersion zero-valent iron particles stabilized by artificial humic acid for lead ion removal. Journal of Hazardous Materials 383, 121170.

Dutta, T., Bagchi, D., Bera, A., Das, S., Adhikari, T., Pal, S.K. Surface engineered ZnO-humic/citrate interfaces: photoinduced charge carrier dynamics and potential application for smart and sustained delivery of Zn micronutrient. 2019. ACS Sustainable Chem. Eng. 712, 10920-10930.

Dvoranová, D., Barbieriková, Z., Brezová, V., 2014. Radical Intermediates in Photoinduced Reactions on TiO_2 (An EPR Spin Trapping Study). Molecules 19, 17279–17304.

Feigin, L. A., Svergun, D. I., 1987. Structure analysis by small-angle X-ray and neutron scattering. Vol. 1. New York: Plenum press.

Guan, X.H., Chen, G.H., Shan, C., 2007. ATR-FTIR and XPS study on the structure of complexes formed upon the adsorption of simple organic acids on aluminum hydroxide, Journal of Environmental Sciences 19, 438–443.

He, X., Sanders, S., Aker, W. G., Lin, Y., Douglas, J., Hwang, H., 2016. Assessing the effects of surface-bound humic acid on the phototoxicity of anatase and rutile TiO2 nanoparticles in vitro. Journal of Environmental Sciences 42, 50-60.

Heuer-Jungemann, A., Feliu, N., Bakaimi, I., Hamaly, M., Alkilany, A., Chakraborty, I., Masood, A., Casula, M.F., Kostopoulou, A., Oh, E., Susumu, K., Stewart, M.H., Medintz, I.L., Stratakis, E., Wolfgang, J., Parak, W.J., Kanaras, A.G., 2019. The role of ligands in the chemical synthesis and applications of inorganic nanoparticles. Chemical reviews 119, 4819-4880.

Huang, Z., Zeng, Z., Song, Z., Chen, A., Zeng, G., Xiao, R., He, K., Yuan, L., Chen, H. Li, G., 2020. Antimicrobial efficacy and mechanisms of silver nanoparticles against Phanerochaete chrysosporium in the presence of common electrolytes and humic acid. Journal of Hazardous Materials 383, 121153.

Jarvie, H.P., King, S. M., 2007. Small-Angle Neutron Scattering Study of Natural Aquatic Nanocolloids. Environ. Sci. Technol. 41, 2868-2873.

JCPDS, International Centre for Diffraction Data (1998)

Jezierski, A., Czechowski, F., Jerzykiewicz, M., Drozd, J., 2000. Electron paramagnetic resonance (EPR) studies on stable and transient radicals in humic acids from compost, soil, peat and brown coal, Spectrochimica Acta Part A Molecular and Biomolecular Spectroscopy 56, 379-385.

Klavins, M., Purmalis, O., 2010. Humic substances as surfactants. Environ. Chem. Lett. 8, 349-354.

Klüpfel, L., Piepenbrock, A., Kappler, A., Sander, M., 2014. Humic substances as fully regenerable electron acceptors in recurrently anoxic environments. Nature Geoscience 7, 195-200.

Kučerík, J., Bursáková, P., Průšová, A., Grebíková, L., Schaumann, G.E., 2012. Hydration of humic and fulvic acids studied by DSC. J. Therm. Anal. Calorim. 110, 451–459.

Li, X., Wu, B., Zhang, Q., Liu, Y., Wang, J., Li, F., Ma, F., Gu, Q., 2020. Complexation of humic acid with Fe ions upon persulfate/ferrous oxidation: Further insight from spectral analysis. Journal of Hazardous Materials 399, 123071.

Lin, D., Ji, J., Long, Z., Yang, K., Wu, F. 2012. The influence of dissolved and surface-bound humic acid on the toxicity of TiO_2 nanoparticles to Chlorella sp. Water Research 46, 4477-4487.

Liu, Y., Zhi, L., Zhou, S., Xie, F., 2020. Effects of mercury binding by humic acid and humic acid resistance on mercury stress in rice plants under high Hg/humic acid concentration ratios. Environ. Sci. and Pollut. Res., https://doi.org/10.1007/s11356-020-08328-9.

Lomakin, A., Teplow, D.B., Benedek, G. B., 2005. Quasielastic light scattering for protein assembly studies, E.M. Sigurdsson (Ed.), Amyloid Proteins: Methods And Protocols, vol. 299, Humana Press, Totowa, New Jearsey.

Luchini, A., Vitiello, G., 2019. Understanding the nano-bio interfaces: lipid-coatings for inorganic nanoparticles as promising strategy for biomedical applications. Frontiers in Chemistry 7, 343.

Luchini, A., Heenan, R.K., Paduano, L., Vitiello, G. Functionalized SPIONs: The surfactant nature modulates the self-assembly and cluster formation. Physical Chemistry Chemical Physics, 2016, 18, 18441-18449.

Luo, X., Shen, L., Meng, F. 2019. Response of microbial community structures and functions of nitrosifying consortia to biorefractory humic substances. ACS Sustainable Chemistry & Engineering 75, 4744-4754.

Maccarthy, P. 2001. The principles of humic substances: an introduction to the first principle, Soil Sci. 166, 738–751.

Mahmoud, M.E., El-Ghanam, A.M., Mohamed, R.H., Saad, S.R., 2020. Enhanced adsorption of Levofloxacin and Ceftriaxone antibiotics from water by assembled composite of nanotitanium oxide/chitosan/nano-bentonite. Mater. Sci. Engin. C 108, 110199.

Mazzei, P., Vinale, F., Woo, S. L., Pascale, A., Lorito, M., Piccolo, A., 2016. Metabolomics by H-HRMAS-NMR of tomato plants treated with two secondary metabolites isolated from Trichoderma. J. Agric. Food Chem. 64, 3538-3545.

Melone, P., Vitiello, G., Di Napoli, M., Zanfardino, A., Caso, M.F., Silvestri, B., Varcamonti, M., D'Errico, G., Luciani, G., 2019. Citric Acid Tunes the Formation of Antimicrobial Melanin-Like Nanostructures. Biomimetics 4, 40.

Nain, B A., Tseng, Y. T., Wei, S. C., Periasamy, A. P., Huang, C. C., Tseng, F. G., Chang, H.T., 2020. Capping 1,3-propanedithiol to boost the antibacterial activity of protein-templated copper nanoclusters. Journal of Hazardous Materials 389, 121821.

Nebbioso, A., Piccolo, A., 2011. Basis of a humeomics science: chemical fractionation and molecular characterization of humic biosuprastructures. Biomacromolecules 12, 1187-99.

Nebbioso A., Piccolo A. 2013. Molecular characterization of dissolved organic matter (DOM): a critical review. Analytical and Bioanalytical Chemistry, 405, 109–124.

Nuzzo, A., Sánchez, A., Fontaine, B., Piccolo, A. Conformational changes of dissolved humic and fulvic superstructures with progressive iron complexation, 2013. Journal of Geochemical Exploration 129, 1-5.

Nuzzo, A., Madonna, E., Mazzei, P., Spaccini, R., Piccolo, A., 2016. In situ photo-polymerization of soil organic matter by heterogeneous nano-TiO_2 and biomimetic metal-porphyrin catalysts. Biol. Fertil. Soils 52, 585–593.

Panzella, L., D'Errico, G., Vitiello, G., Perfetti, M., Alfieri, M.L., Napolitano, A., D'Ischia, M., 2018. Disentangling structure-dependent antioxidant mechanisms in phenolic polymers by multiparametric EPR analysis, Chem. Commun. 54, 9426–9429.

Pecora, J. B. R., 2003. Dynamic Light Scattering: With Applications to Chemistry, Biology and Physics Couvire Dover Publications.

Peña-Méndez, M.E., Havel, J.; Patočka, H. Humic substances - compounds of still unknown structure: applications in agriculture, industry, environment, and biomedicine. 2005. J. Appl. Biomed. 3, 13-24.

Perminova, I.V., García-Mina, J.M., Knicker, H., Miano, T. 2019. Humic substances and nature-like technologies. J. Soils Sediments 19, 2663-2664.

Pezzella, A., Capelli, L., Costantini, A., Luciani, G., Tescione, F., Silvestri, B., Vitiello, G., Branda, F., 2013. Towards the development of a novel bioinspired functional material: synthesis and characterization of hybrid TiO_2/DHICA-melanin nanoparticles. Mater. Sci. Engin. C 3, 347-355.

Piccolo, A., 2001. The supramolecular structure of humic substances. Soil Science 166, 810-832.

Piccolo, A., Spaccini, R., Savy, D., Drosos; M., Cozzolino, V. 2019. The soil humeome: chemical structure, functions and technological perspectives. In: Sustainable agrochemistry: a compendium of technologies. Ed: Vaz S. jr., Springer Nature, Heidelberg, pp. 183-222.

Piccolo, A., Conte, P., Tagliatesta, P., 2005. Increased conformational rigidity of humic substances by oxidative biomimetic catalysis. Biomacromolecules 6, 351-358.

Piccolo, A., Conte, P., Cozzolino, A., 1999. Effects of mineral and monocarboxylic acids on the molecular association of dissolved humic substances. European Journal of Solid Science 50, 687-694.

Pirozzi, D., Imparato, C., D'Errico, G., Vitiello, G., Aronne, A., Sannino, F., 2020. Three-year lifetime and regeneration of superoxide radicals on the surface of hybrid TiO_2 materials exposed to air. Journal of Hazardous Materials 387, 121716.

Phoon, B. L., Ong, C. C., Shuai, M., Saheed, M., Show, P. L., Chang, J. S., Ling, T. C., Lami, S. S., Juan, J. C., 2020. Conventional and emerging technologies for removal of antibiotics from wastewater. Journal of Hazardous Materials 400, 122961.

Pota, G., Venezia, V., Vitiello, G., Di Donato, P., Mollo, V., Costantini, A., Avossa, J., Nuzzo, A., Piccolo, A., Silvestri, B., Luciani, G., 2020. Tuning functional behavior of humic acids through interactions with Stöber silica nanoparticles, Polymers 12, 982.

Rainer, A., Rochus, W., 1978. Studies on the antimicrobial effect of natural and synthetic humic acids. Arzneimittel-Forschung/Drug Research 28, 2195-2198.

Roscigno, P., Paduano, L., D'Errico, G., Vitagliano, V., 2001. On the presumed specific interaction of anionic surfactants with nonionic polymers. Aqueous solution of sodium alkylsulfonate in the presence of poly(vinylpyrrolidone): an "excluded volume" effect. Langmuir 17, 4510-4518.

Scott, D.T., Mcknight, D.M., Blunt-Harris, E.L., Kolesar, S.E., Lovley, D.R., 1998. Quinone moieties act as electron acceptors in the reduction of humic substances by humics reducing microorganisms. Environ. Sci. Technol. 32, 2984-2989.

Sibley, S.D., Pedersen, J.A., 2008. Interaction of the macrolide antimicrobial clarithromycin with dissolved humic acid, Eviron. Sci. Technol. 42, 422–428.

Silvestri, B., Armanetti, P., Sanità, G., Vitiello, G., Lamberti, A.c Calì, G., Pezzella, A., Luciani, G., Menichetti, L., Luin, S., d'Ischia, M., 2019. Silver-nanoparticles as plasmon-resonant enhancers for eumelanin's photoacoustic signal in a self-structured hybrid nanoprobe. Mater. Sci. and Engin. C 102, 788-797.

Spaccini, R., Cozzolino, V., Di Meo, V., Savy, D., Drosos, M., Piccolo, A. 2019. Bioactivity of humic substances and water extracts from compost made by ligno-cellulose wastes from biorefinery. Sci. of The Total Environ. 646, 792-800.

Song, M., Song, B., Meng, F., Chen, D., Sun, F., Wei, Y., 2019. Incorporation of humic acid into biomass derived carbon for enhanced adsorption of phenol. Scientific Reports 9, 19931.

Stan, M., Lung, I., Soran, M. L., Leostean, C., Popa, A., Stefan, M., Lazar, M.D., Opris, O. Silipas, T.D., Porav, A. S., 2017. Removal of antibiotics from aqueous solutions by green synthesized magnetite nanoparticles with selected agro-waste extracts. Process Safety and Environmental Protection 107, 357-372.

Stevenson, F.J. 1994. Humus Chemistry: Genesis, Composition, and Reactions, 2nd edn. Wiley Interscience, New York.

Tang, W.W., Zeng, G.M., Gong, J.L., Liang, J., Xu, P., Zhang, C., Huang, C.C., 2014. Impact of humic/fulvic acid on the removal of heavy metals from aqueous solutions using nanomaterials: A review. Science of the Total Environment 468–469, 1014–1027.

Tikhonov, V.V., Yakushev, A.V., Zavgorodnyaya, Y. A., Byzov, B. A., Demin, V.V., 2010. Effects of humic acids on the growth of bacteria. Eurasian Soil Science, 43, 305–313.

van Rensburg, C. E. J., van Straten, A., Dekker, J., 2000. An *in vitro* investigation of the antimicrobial activity of oxifulvic acid. Journal of Antimicrobial Chemotherapy 46, 853-885.

Venezia, V., Sannino, F., Costantini, A., Silvestri, B., Cimino, S., Califano, V., 2020. Mesoporous silica nanoparticles for β-glucosidase immobilization by templating with a green material: Tannic acid. Micropor. Mesopor. Mat. 110203.

Villamena, F.A., Zweier, J. L., 2004. Detection of Reactive Oxygen and Nitrogen Species by EPR Spin Trapping. Antioxidants & Redox Signaling. 6, 3.

Vitiello, G., Pezzella, A., Zanfardino, A., Varcamonti, M., Silvestri, B., Costantini, A., Branda, F., Luciani, G., 2015. Titania as a driving agent for DHICA polymerization: a novel strategy for the design of bioinspired antimicrobial nanomaterials. J. Mater. Chem. B 3, 2808-2815.

Vitiello, G., Pezzella, A., Calcagno, V., Silvestri, B., Raiola, L., D'Errico, G., Costantini, A., Branda, F., Luciani, G., 2016. 5,6-Dihydroxyindole-2-carboxylic acid-TiO_2 charge transfer complexes in the radical polymerization of melanogenic precursor(s). J. Phys. Chem. C 120, 6262-6268.

Vitiello, G., Pezzella, A., Zanfardino, A., Silvestri, B., Giudicianni, P., Costantini, A., Varcamonti, M., Branda, F., Luciani, G., 2017. Antimicrobial activity of eumelanin-based hybrids: The role of TiO_2 in modulating the structure and biological performance. Mater. Sci. Engin. C 75, 454-462.

Vitiello, G., Zanfardino, A., Tammaro, O., Di Napoli, M., Caso, M. F., Pezzella, A., Varcamonti, M., Silvestri, B., D'Errico, G., Costantini, A., Luciani, G., 2018. Bioinspired hybrid eumelanin-TiO_2 antimicrobial nanostructures: the key role of organo-inorganic frameworks in tuning eumelanin's biocide action mechanism through membrane interaction. RSC Adv. 8, 28275-28283.

Vitiello, G., Melone, P., Silvestri, B., Pezzella, A., Di Donato, P., D'Errico, G., Di Napoli, M., Zanfardino, A., Varcamonti, M., Luciani, G., 2019. Titanium based complexes with melanin precursors as a tool for directing melanogenic pathways. Pure and Applied Chem. 91, 1605–1616.

Wenk, H. R., 2018. Neutron Scattering in Earth Sciences. Walter de Gruyter GmbH & Co KG.

Xu, B., Lian, Z., Liu, F., Yu, Y., He, Y., Brookes, P.C., Xu, J., 2019. Sorption of pentachlorophenol and phenanthrene by humic acid-coated hematite nanoparticles. Environmental Pollution 248, 929-937.

Xu, C., Nasrollahzadeh, M., Selva, M., Issaabadi, Z., Luque, R., 2019. Waste-to-wealth: biowaste valorization into valuable bio(nano)materials. Chem. Soc. Rev. 48, 4791-4822.

Yarkova, T. A. (2011 Chemical modification of humic acids by the introduction of indole-containing fragments. Solid Fuel Chemistry 45, 261-266.

Zanfardino, A., Restaino, O. F., Notomista, E., Cimini, D., Schiraldi, C., De Rosa, M., De Felice, M., Varcamonti, M., 2010. Research Isolation of an Escherichia coli K4 kfoC mutant over-producing capsular chondroitin. Microbial Cell Factories 9, 34.

Zhang, H., Annunziata, O., 2008. Effect of Macromolecular Polydispersity on Diffusion Coefficients Measured by Rayleigh Interferometry. J. Phys. Chem. B 112, 3633-3643.

Zhang, M., Li, D., Ye, Z., Wang, S., Xu, N., Wang, F., Liu, S., Chen, J., Gu, H. Effect of humic acid on the sedimentation and transport of nanoparticles silica in water-saturated porous media. J. Soils Sediments 20, 911–920.

Zhao, T., Fang, M., Tang, Z., Zhao, X., Wu, F., Giesy, J.P., 2019. Adsorption, aggregation and sedimentation of titanium dioxide nanoparticles and nanotubes in the presence of different sources of humic acids. Sci. Total Environ. 692, 660-668.